Geophysical Research Letters

RESEARCH LETTER
10.1029/2023GL106471

Special Collection:
The Perseverance Rover's Exploration of the Western Fan Front, Jezero Crater, Mars

Assessing Radar Attenuation in RIMFAX Soundings at the Jezero Western Fan Front, Mars

Sigurd Eide[1], Titus M. Casademont[1], Emileigh S. Shoemaker[2,3], Sverre Brovoll[1,4], Tor Berger[1,4], Henning Dypvik[1], and Svein-Erik Hamran[1]

[1]Centre for Space Sensors and Systems (CENSSS), University of Oslo, Kjeller, Norway, [2]Lunar and Planetary Laboratory, University of Arizona, Tucson, AZ, USA, [3]Now at NASA Goddard Space Flight Center, Greenbelt, MD, USA, [4]Norwegian Defence Research Establishment (FFI), Kjeller, Norway

Key Points:

- The first estimate of radar attenuation at the Jezero Western Fan Front is on average −2.1 dB/m
- For an average propagation velocity of 0.113 m/ns, returned power and time-frequency analyses yield similar results
- Radar properties are consistent with dry sedimentary rocks and are distinguishable from the magmatic lithologies on Jezero Crater Floor

Correspondence to:
S. Eide,
sigurd.eide@its.uio.no

Citation:
Eide, S., Casademont, T. M., Shoemaker, E. S., Brovoll, S., Berger, T., Dypvik, H., & Hamran, S.-E. (2024). Assessing radar attenuation in RIMFAX soundings at the Jezero western fan front, Mars. *Geophysical Research Letters*, *51*, e2023GL106471. https://doi.org/10.1029/2023GL106471

Received 21 SEP 2023
Accepted 22 MAY 2024

Author Contributions:
Conceptualization: Sigurd Eide, Svein-Erik Hamran
Data curation: Sigurd Eide
Formal analysis: Sigurd Eide, Titus M. Casademont, Sverre Brovoll
Funding acquisition: Svein-Erik Hamran
Investigation: Sigurd Eide, Titus M. Casademont
Methodology: Sigurd Eide, Sverre Brovoll, Svein-Erik Hamran
Project administration: Svein-Erik Hamran

Abstract Estimates of radar attenuation in the shallow Martian subsurface are retrieved from RIMFAX soundings along the Perseverance rover traverse. Specifically, analyzed data is from the Hawksbill Gap area during the rover's first drives onto the Jezero Western Fan Front. The centroid frequency-shift method is employed to quantify attenuation in terms of the constant-Q approximation. Results are then compared with the amplitude decay method, which—in order to calculate attenuation—requires propagation velocities retrieved from radargram analysis. By verifying that results from two separate analyses are consistent, we ensure that quantified radar properties are well constrained. First estimate of constant-Q is 78.8 ± 11.6. For a subsurface propagation velocity of 0.113 m/ns, that equals an attenuation of −2.1 ± 0.4 dB/m at the RIMFAX 675 MHz center frequency. Results are consistent with dry sedimentary rocks, and are distinguishable from the magmatic lithologies on Jezero Crater Floor.

Plain Language Summary This study presents first estimates of radar attenuation at the Jezero Western Fan Front. Measurements were made with the RIMFAX payload instrument on the Mars 2020 Perseverance rover mission, acquired along the rover drive path. Results indicate low signal losses in the subsurface that are consistent with dry sedimentary rocks, as observed on the surface by other payload instruments. Maximum imaging depths increase compared to imaging over magmatic lithologies on Jezero Crater Floor. By using separate methods of analysis (the centroid frequency-shift method and the amplitude decay method), we reliably quantify attenuation and maximum penetration depths at the Western Fan Front, and observe differences to the Crater Floor lithologies.

1. Introduction

During sols 439–538 of NASA's Perseverance rover mission on Mars, the first drive was conducted onto Hawksbill Gap, at the lower parts of Jezero Western Fan (JWF). Later on sol 698, departing from the same location, the rover initiated its traverse across the JWF. The sedimentary fan succession has a distinct geomorphology compared to the magmatic lithologies present on the Crater Floor, and JWF had in fact been identified as a prime scientific target prior to mission start (e.g., Stack et al., 2020). In previous literature, JWF has also been referred to as Jezero Western Delta. The Radar Imager for Mars' Subsurface Exploration (RIMFAX; Hamran et al., 2020) acquired measurements all along while the Perseverance rover drove on top of this sedimentary deposit.

Analyzing attenuation in the radar soundings can disclose key subsurface properties of JWF that will be complementary to principle radargram interpretations presented in Paige et al. (2024). It is also interesting to compare attenuation estimates to those from the Crater Floor (Eide et al., 2022), and identify similarities and differences between distinct terrains. It was observed during initial RIMFAX sounding over JWF, that imaging depths increased compared to the Crater Floor (Paige et al., 2024). In this study we aim at quantifying the difference in attenuation, focusing on the upper 5–7 m below the surface as recorded in the RIMFAX Shallow Mode, operating in the frequency range 150–1,200 MHz.

Ground-penetrating radar (GPR) data is strongly affected by the frequency dependent attenuation mechanisms that cause subsurface reflections to be weakened and broadened compared to the transmitted waveform. The constant-Q factor was originally used to describe similar behavior for seismic waves, due to cumulative attenuating effects in the ground (Richards & Aki, 1980), but it was also found applicable for electromagnetic

Software: Sigurd Eide, Titus M. Casademont, Sverre Brovoll, Tor Berger, Svein-Erik Hamran
Supervision: Tor Berger, Henning Dypvik, Svein-Erik Hamran
Validation: Sigurd Eide, Titus M. Casademont, Sverre Brovoll
Visualization: Sigurd Eide, Titus M. Casademont
Writing – original draft: Sigurd Eide, Emileigh S. Shoemaker, Henning Dypvik, Svein-Erik Hamran
Writing – review & editing: Sigurd Eide, Emileigh S. Shoemaker, Henning Dypvik, Svein-Erik Hamran

propagation in natural soil and rocks over the GPR frequency range 0.1–1.0 GHz (Turner & Siggins, 1994). Many radar studies assume that the constant-Q model or equivalent is appropriate (Bradford, 2007; Campbell et al., 2008; Irving & Knight, 2003; Lauro et al., 2017), and—in particular—it has gained recent interest in planetary rover science (Chen et al., 2023; Ding et al., 2020; Eide et al., 2022).

Common notation for GPR make use of the generalized parameter Q* (Turner & Siggins, 1994), which can be used to describe the attenuation constant α:

$$\alpha = \frac{\omega}{2Q^* v}[Np/m] = 8.69 \times \frac{\omega}{2Q^* v}[dB/m]. \quad (1)$$

The model assumes that the attenuation constant is linearly related the angular frequency ω. The variable v represents the radar wave propagation velocity. Attenuation can alternatively be described in terms of the "effective loss tangent" (tan $\delta_e = 1/Q^*$).

In this study, we first derive subsurface radar attenuation through the centroid frequency-shift (CFS) method (Quan & Harris, 1997), and then assess the results with the amplitude decay (AD) method (Tonn, 1991). Whereas relative change in spectral components by the CFS-method provide a measure of attenuation without additional presumptions, returned power estimates with the AD-method require compensation of acquisition parameters and input of the subsurface propagation velocity. Accordingly, we use returned power estimates to assess whether retrieved radar properties are well constrained.

Sols 439–538 and 698–709 are analyzed in this study, covering the first drive onto JWF and the start of the larger traverse across the whole fan unit, Figure 1. Only soundings from the Hawksbill Gap area are studied, while other areas investigated by the Perseverance rover are not considered (including other parts of JWF and areas close to the fan escarpment on the Crater Floor). Velocity estimates from the area are available in Paige et al. (2024), acquired through radargram travel-time analysis by hyperbolic fitting to diffractions. By conducting two separate analyses (CFS and AD), attenuation estimates can reliably be quantified and any differences between JWF and the Crater Floor can be assuredly detected.

2. Methods

2.1. Propagation Velocity Estimates

Estimates of propagation velocities over the Jezero Western Fan Front (JWF Front), are presented by Paige et al. (2024), acquired through travel-time hyperbolic fitting to point diffractions as in Casademont et al. (2023). The analysis gives 0.113 ± 0.013 m/ns, based on 11 hyperbolas in the upper 12 m of the radargrams, with an average diffraction depth of 3.12 m. Velocity estimates are based on RIMFAX Deep Mode operating in the frequency range 150–600 MHz, which we assume will also be valid for the Shallow Mode soundings with the full RIMFAX bandwidth analyzed in this study. The results can also be presented in terms of the relative permittivity $\varepsilon' = c^2/v^2 = 7.18 \pm 1.32$ (with "v" being the propagation velocity in the subsurface and "c" being the speed of light in free space).

2.2. Attenuation Analysis With the Centroid Frequency-Shift Method

The CFS method (Quan & Harris, 1997) is employed as in Eide et al. (2022). A single estimate of the Q*-factor can be derived analytically from the slope $\Delta f_c/\Delta t$, which is a best-fit to the change in center frequency f_c in the time-frequency spectra of a recording:

$$Q^* = -C\pi\left(\frac{\Delta f_c}{\Delta t}\right)^{-1}, \quad (2)$$

where Δt is a two-way travel-time (TWT) interval. The TWT range analyzed is 25–125 ns. A final Q*-value for a section of a radargram, is an averaged value of several statistically independent estimates. In this study, a Q*-value is estimated every 5 m along the rover track and—ultimately—the average from 100s of estimated Q*-values will be descriptive of an area.

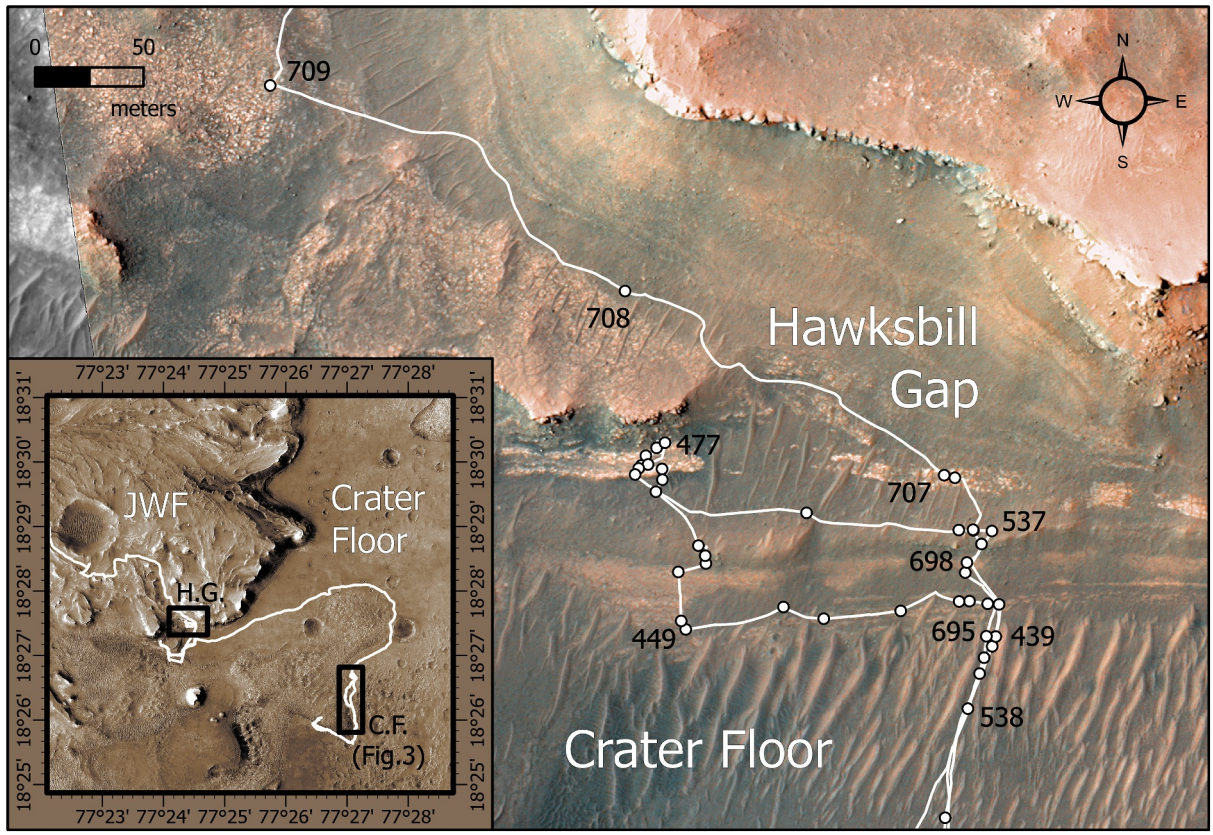

Figure 1. Map view over RIMFAX soundings acquired in the Hawksbill Gap area during sols (i) 439–538 and (ii) 698–709. The first drives on top of Jezero Western Fan (JWF) was made during (i), while (ii) was the start of the longer traverse across it. Sol numbering indicated on the map are "end of drive" locations. The basemap is a Mars 2020 Science Team colored HiRISE mosaic. Inset figure on lower left is a false-colored HiRISE mosaic and indicates with a black outline the location of the study area (annotated "H.G."). Also indicated is the Crater Floor site used for testing the analysis that is presented in Figure 3 (annotated "C.F./Figure 3").

2.3. Attenuation Analysis With the Amplitude Decay Method

The amplitude decay (AD) method (Tonn, 1991) is employed to retrieve a Q*-value by analyzing the change in amplitude with travel-time. Similarly to the CFS-method, a Q*-value is obtained for every 5 m along the rover track, Figure 2a. The time-domain radargram is generated from the recorded deramped data as described in Eide et al. (2022): background removal; spectral enhancement; amplitude tapering; and Fast Fourier Transform. In (b), the average power return for a 5 m radargram section is displayed.

The AD-method then require correction for (i) acquisition gating used in RIMFAX and (ii) geometrical spreading. (i) Acquisition gating is described in Hamran et al. (2020) and can be corrected for by multiplication of the reciprocal of the resulting gating response, Figures 2c and 2d.

Theoretically, the electric field strength amplitude E of the received signal after gating corrections can be written as:

$$E = \frac{E_0}{2\tilde{r}} \times \exp\left(-\frac{\omega(t - t_s)}{2Q^*}\right). \quad (3)$$

The reference field strength E_0 is at the point of radiation. TWT is denoted t, and t_s is the surface reflection delay in TWT. The apparent target range is written $\tilde{r}$, while $2\tilde{r}$ is the apparent traveled distance. The word "apparent" is used to incorporate a geometrical effect: For an air-coupled antenna elevated off the ground to an height h_0, a depth dependent gain will be caused by refraction at the surface. For an idealized homogeneous subsurface with propagation velocity v, and c being the speed of light, the apparent range and TWT is related by the far-field optical solution:

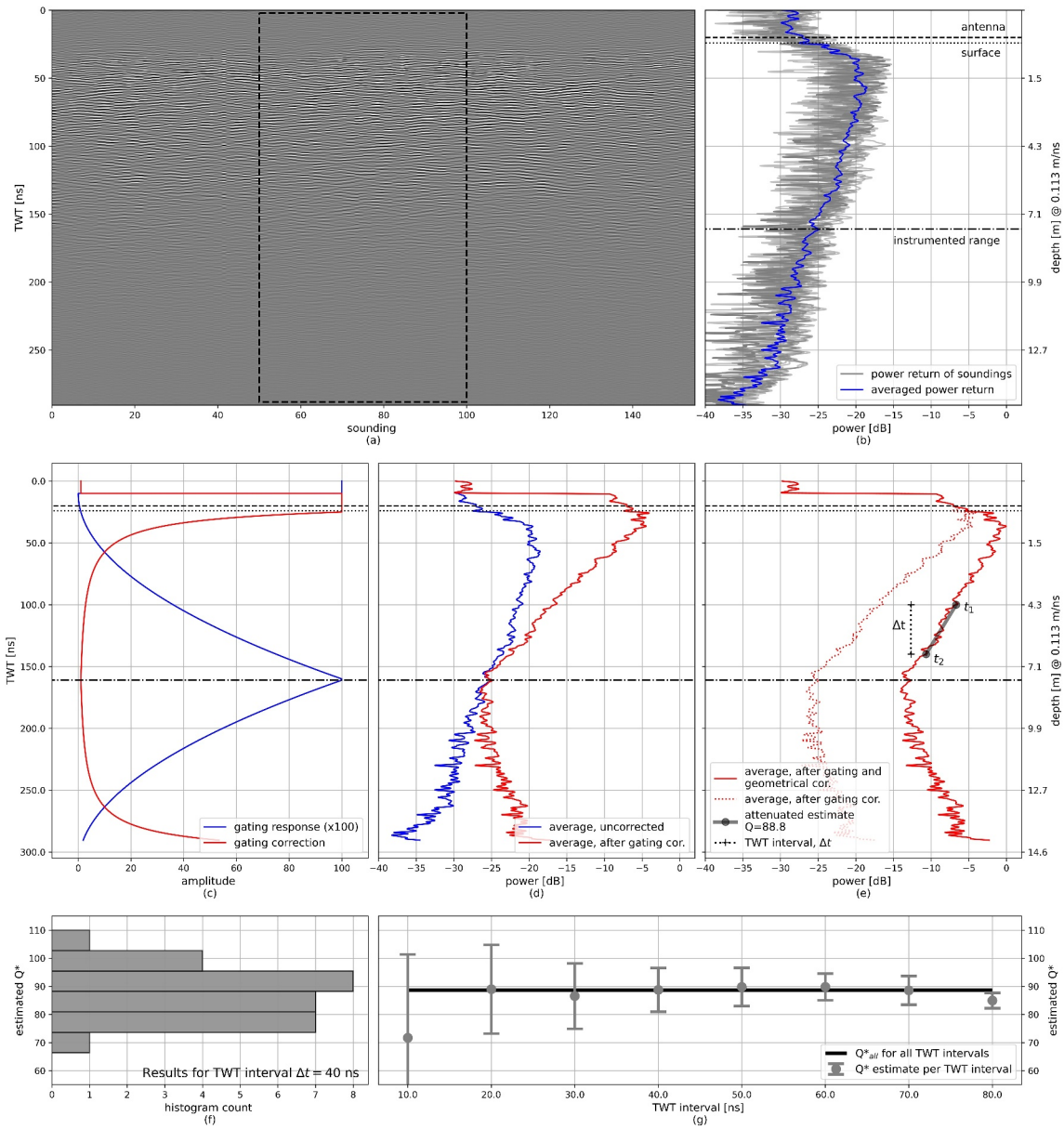

Figure 2. Example of returned power analysis for RIMFAX Shallow Mode from sol 474. (a) Radargram superimposed by a rectangular selection outlining data analyzed per Q* estimate (5 m along track distance). Horizontal axis is in soundings, taken 10 cm apart along the rover drive path. Vertical axis is in TWT, or—alternatively—depth below ground. (b) Power return for all individual soundings in selection (gray) and the average (blue). The averaged power return has also been applied a median filter for smoothing. Delay times for "antenna," "surface" and "instrumented range" are added for reference (see Hamran et al. (2020) for their description). (c) The gating response in blue (multiplied with 100 for display purposes) and the reciprocal correction function in red, with a cut off gain at +20 dB. (d) Comparison of power in radargram before and after gating correction. (e) Returned power before and after correction for geometrical spreading. A single attenuation estimate is included for a 40 ns two-way travel-time (TWT) interval between t_1 and t_2, yields Q* = 88.8. (f) Histogram plot for estimating Q* for 40 ns TWT intervals, where several estimates are obtained by sliding the TWT interval at 2 ns increments, between 50 and 150 ns. (g) Q* estimates for TWT intervals between 10 and 80 ns in gray, with uncertainties described in terms of the semi-IQR. Marked in a thick black line is Q^*_{all}, the median of all TWT interval Q* estimates, which is the final result from the attenuation analysis of the selected radargram section.

$$2\tilde{r} = 2h_0 + 2z\left(\frac{v}{c}\right) = 2h_0 + \frac{v^2(t - t_s)}{c}. \tag{4}$$

This correction is in accordance with the "refraction gain" (or "lensing effect") in radioglaciology (Bogorodsky et al., 1985), or—similarly—the "divergence effects" in reflection seismology (Newman, 1973). Whereas negligible refraction gain would yield the range r as $r = h_0 + z = h_0 + v(t - t_s)/2$. In this study, refraction gain is

assumed according to Equation 4 and is in-fact consistent with assumptions made during derivation of the propagation velocities in the travel-time analysis (Casademont et al., 2023).

Geometrical spreading is furthermore assumed similar to nadir sounding and reflection at planar layers, contrary to point scatterers commonly used in power calculations with, for example, the "radar equation." Therefore, geometrical spreading for two-way propagation and reflection is approximated with $2\tilde{r}$ instead of $\tilde{r}^2$ (Ulaby & Long, 2014), as found suitable for describing power return in nadir subsurface sounding (e.g., Eide et al., 2021).

For a recording where the signal amplitudes have been corrected for (i) gating and (ii) geometrical spreading, the corrected electrical field strength $\tilde{E}_{t_i}$ at a TWT t_i, is written in terms of its apparent traveled distance $2\tilde{r}_i$: $\tilde{E}_{t_i} = E_{t_i} \times 2\tilde{r}_i$. Attenuation can then be obtained directly from looking at the amplitude decay over a TWT interval Δt between t_1 and t_2 (Tonn, 1991):

$$Q^* = \pi f_c \Delta t \left(\ln \frac{\tilde{E}_{t_1}}{\tilde{E}_{t_2}} \right)^{-1}. \tag{5}$$

In Figure 2e the amplitudes are plotted in dotted line before geometrical correction, and solid line after. A single Q*-estimate is also illustrated over a TWT interval.

Figures 2f and 2g furthermore present a more robust algorithm for estimating Q*, by averaging over a combination of TWT intervals. In (f), Q* has been estimated for 40 ns TWT intervals, in the TWT range from 50 to 150 ns. A Q* value is calculated for every 40 ns interval, at 2 ns steps. Valid results ($0 < Q^* < 200$) are plotted in a histogram and show the spread in obtained values. In (g), the median and semi-interquartile range (semi-IQR) for TWT intervals between 10 and 80 ns are plotted. The final result from analyzing the 5 m wide radargram selection, is described in terms of the median of all the TWT-interval results.

Assumptions in the AD analysis are that reflections will be evenly distributed in the recording, and that the respective targets will have equal reflectivity (i.e., the same "radar cross section"). Then the decay in returned power over a time interval will be an effect of attenuation alone, after having corrected for acquisition and geometrical spreading. By a statistical approach, we try to meet these assumptions. In Figure 2b, the power return is averaged over many neighboring soundings making a smooth returned power with travel-time curve. Furthermore, averaging is done over many estimates: for each TWT interval as in (f), and between a range of intervals as in (g). It can be seen how the final result is a combination of averages with outliers being removed at each step.

2.4. Assessing Estimates of Radar Attenuation and Propagation Velocity From Jezero Crater Floor

We chose a well-studied area along the Perseverance traverse as a test site for comparing results from the CFS and AD methods. We focus on the Eastern part of the Crater Floor containing traverses from sols 15–135 and 354–379, Figure 3a. RIMFAX data from this area has been interpreted in Hamran et al. (2022), and quantification of radar attenuation has already been done with the CFS-method (Eide et al., 2022). Velocity estimates are available in Casademont et al. (2023). For both subsurface parameters, however, there are great variation in the estimated values, so the average of many estimates are considered representative for the area.

In Figure 3b are the obtained estimates from the CFS-method ($Q^* = 71.9 \pm 8.3$). In (c) are velocity estimates ($v = 0.108 \pm 0.023$ m/ns), which differ slightly from those published for the whole Crater Floor ($v = 0.10 \pm 0.02$ m/ns). Estimates by the AD-method is presented in (d), employing the average propagation velocity and comparing different geometrical corrections. The difference between the corrections $\tilde{r} = h_0 + z(v/c)$ and $r = h_0 + z$, is quite small and within the uncertainty of the analyses. Both assume nadir sounding and reflections from planar layering. The r^2 correction is typically employed in geometrical corrections for point scatterers, however, from the Q*-estimates, it is apparent that approximation for planar layers is more appropriate in this analysis.

In (e), employing the geometrical correction from Equation 4, a comparison is done for Q*-estimates using different velocities (the average, and one standard deviation above and below). Using the average velocity, the AD-method yields $Q^* = 69.1 \pm 5.5$. For a velocity one standard deviation above the mean, the AD-method yield

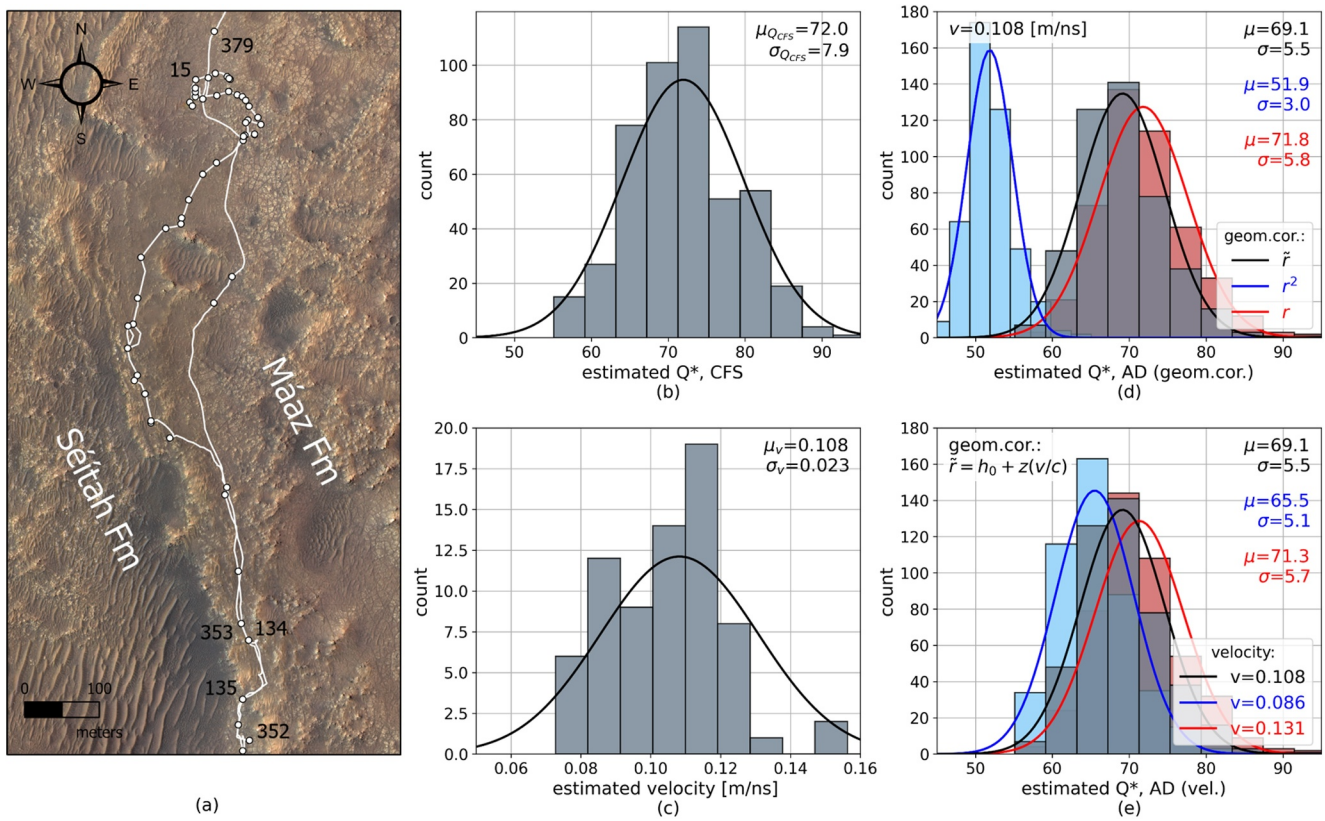

Figure 3. Assessment of Crater Floor estimated properties with the AD-method. (a) Traverse during sols 15–135 and 353–379. (b) Attenuation estimates from the centroid frequency-shift method. (c) Propagation velocity estimates derived from travel-time analysis (Casademont et al., 2023). (d) Attenuation estimates from the AD-method comparing different geometrical corrections, with the propagation velocity equal the mean value of 0.108 m/ns. (e) Attenuation estimates from the AD-method comparing different propagation velocities (the mean and one standard deviation below and above). The geometrical correction used is according to Equation 4.

$Q^* = 71.3 \pm 5.7$ and is in-fact even closer to the CFS results. For a velocity one standard deviation below, the AD-method yield $Q^* = 65.5 \pm 5.1$ and is significantly less than the other estimates.

We observe that using the appropriate geometrical spreading correction during the AD analysis is crucial for retrieving a correct Q*-estimate. Varying the velocity affect the retrieved power return and the calculated attenuation, but the method is not sensitive to small changes. However, when employing a reasonable velocity, the AD-method can assess whether results obtained with the CFS-method are valid. In this comparison for the Jezero Crater Floor, we observe that the averaged subsurface parameters are well constrained. In terms of the relative permittivity and effective loss tangent, the parameters can alternatively be described by $\varepsilon' = 7.7 \pm 4.8$ and $\tan\delta = 0.014 \pm 0.002$, respectively.

3. Results and Discussion

Attenuation estimates are done every 5 m along the rover traverse at the Jezero Western Fan Front (JWF Front). Results form the CFS analysis are $Q^* = 78.8 \pm 11.6$, Figure 4a. That equals tan $\delta_e = 1/Q^* = 0.013 \pm 0.002$, in terms of the effective loss tangent. The Q*-value is higher compared to the results form the Crater Floor (indicating lower attenuation). The spread in estimated values is substantial, as seen in the histogram and from the standard deviation, but this is similar to what observed over the Crater Floor.

Paige et al. (2024) present velocity estimates of 0.113 ± 0.013 m/ns from radargram analysis over JWF, Figure 4b. These estimates are slightly higher than what Casademont et al. (2023) observed over the Crater Floor (0.10 ± 0.02 m/ns). In terms of the relative permittivity, $\varepsilon' = 7.18 \pm 1.32$ over JWF while $\varepsilon' = 8.9 \pm 3.2$ over the Crater Floor.

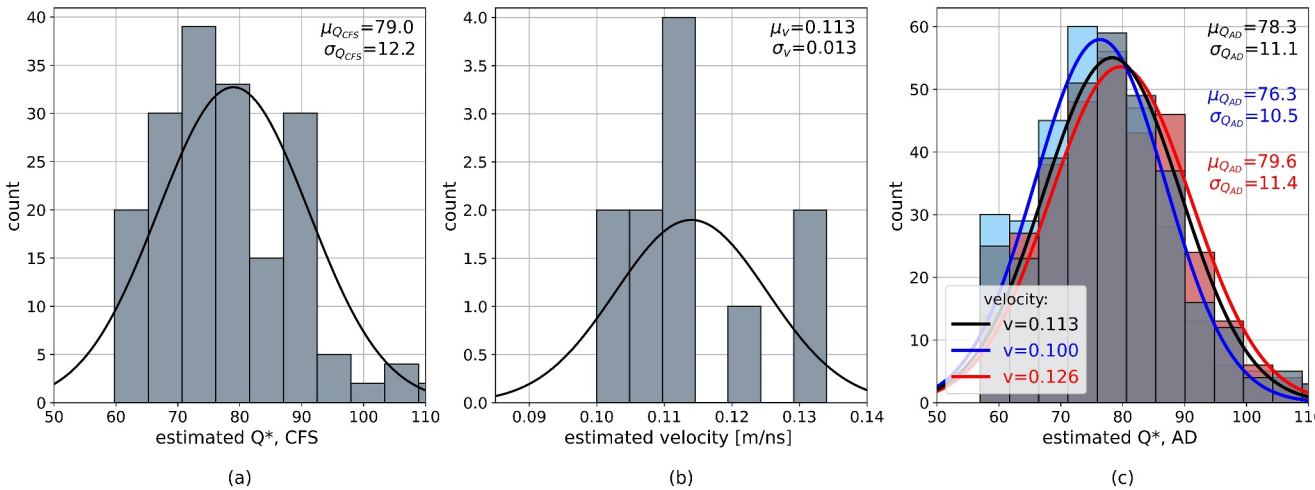

Figure 4. Attenuation estimates for the rover traverse in Figure 1: (a) from the centroid frequency-shift method; (b) propagation velocities from Paige et al. (2024); and (c) attenuation estimates by the AD-method. Mean and standard deviations are listed for each histogram. For the AD analysis in (c), comparison is done between analysis made with the mean velocity, and one standard deviation below and above.

We then employ available velocity estimates in the amplitude decay (AD) analysis, to assess whether it can reproduce similar attenuation as the CFS analysis. In Figure 4c, AD analysis yields Q* = 78.3 ± 11.1 for the mean velocity value. Comparison with one standard deviation below and above yield similar results, though differences are sightly larger toward lower velocities.

Attenuation over JWF is −2.1 ± 0.4 dB/m for calculations at the RIMFAX 675 MHz center frequency, with the average velocity of 0.113 m/ns. Both the CFS and the AD methods yield similar losses in dB. Differences to the Crater Floor are seen in Q*-estimates, but they are further enhanced when calculating the attenuation constant from Equation 1, because the areas have different average velocities. On the Crater Floor, Q* = 70.4 ± 7.7 and $\alpha = -2.6 \pm 0.3$ dB/m.

As in Eide et al. (2022), there are large variations in acquired CFS Q*-estimates. For AD estimates, we have assumed a single constant velocity to be valid over the whole area, which do not account for local variations that in turn would affect estimates of Q*-values. But the fact that the two distinct analyses provide similar Q*-estimates on average, ensures that quantified results are reasonable and that the observed difference between JWF and the Crater Floor is reproducible and statistical significant, despite large and overlapping variances for estimated values.

The constant-Q attenuation model is assumed to be valid over the whole RIMFAX bandwidth, that is, that the attenuation constant has a linear dependency with frequency. There are however other studies (e.g., Harbi & McMechan, 2012) that investigate the frequency dependent attenuation in more detail. That should be interesting for future RIMFAX studies, but is out of scope for this investigation. Nevertheless, since results from both CFS and AD methods are consistent for the areas studied, we conclude the validity of the constant-Q model is still a useful assumption for studying bulk attenuation over the full RIMFAX bandwidth.

3.1. Depth of Penetration

With the System Dynamic Range (Hamran, 2010) assumed the same for RIMFAX soundings over JWF and the Crater Floor, the amount of power loss at maximum depth of penetration ($z^{\max}$) will be equal in the two areas. Therefore, the sum of attenuation $\alpha z^{\max}$ and geometrical spreading loss L^{-1} will be constant:

$$2\alpha_{cf} z_{cf}^{\max} + L(2\tilde{r}_{cf}^{\max})^{-1} = 2\alpha_{\text{jwf}} z_{\text{jwf}}^{\max} + L(2\tilde{r}_{\text{jwf}}^{\max})^{-1}. \quad (6)$$

Geometrical spreading is represented by the free-space propagation loss (Ulaby & Long, 2014), but utilizing the apparent target range $\tilde{r}$:

$$L(\tilde{r})^{-1} = 20\log_{10}\left(\frac{\lambda_0}{4\pi\tilde{r}}\right), \quad (7)$$

where $\lambda_0 = 2\pi c/\omega$. Calculations are done for the RIMFAX center frequency, and the relationship between $\tilde{r}$ and z is as in Equation 4.

We assume attenuation estimates obtained for RIMFAX Shallow Mode, are also valid for the radar configuration used when imaging down to maximum depth of penetration utilizing long integration times and the full instrument bandwidth. For the Crater Floor, we assume $\alpha_{cf} = -2.6$ dB/m (Eide et al., 2022) and $z_{cf}^{\max} = 15$ m (Hamran et al., 2022). For JWF, α_{jwf} is −2.1 dB/m. Solving Equation 6 with respect to $z_{jwf}^{\max}$, we obtain a maximum depth of penetration of ∼18 m. Consequently, imaging depth should increase by about 3 m over JWF, compared to on the Crater Floor. These quantified differences in attenuation and maximum depth of penetration are consistent with processed radargrams from the areas (Hamran et al., 2022; Paige et al., 2024).

3.2. Implications for Regolith Composition

Surface rocks analyzed by the Perseverance rover at JWF, indicate distinct formation compared to on the Crater Floor. Whereas the latter was mainly concluded to have magmatic origin (Farley et al., 2022), JWF is found to represent a sedimentary fan deposit (Stack et al., 2024). The difference in radar propagation velocities between the Crater Floor and JWF, is consistent with change from magmatic lithologies to sedimentary. Furthermore, in general, sounding over sedimentary rocks tend to be less affected by attenuation than sounding over volcanic terrain. The observed lower attenuation in RIMFAX data over the sedimentary rocks of JWF, is therefore consistent with general observations on Earth (e.g., Ulaby & Long, 2014) and observations from orbital sounding of Mars (Campbell et al., 2008). Attenuation is, however, not a direct indicator of composition, and sounding over different regions of sedimentary origin would be expected to yield a large variation in the results.

Comparing RIMFAX results directly with orbital radar measurements has to be done with care: While Campbell et al. (2008) analyze SHARAD data acquired during orbital sounding with a 20 kHz center frequency and a km-wide spatial footprint, RIMFAX is operating at the surface with a 675 MHz center frequency. Nevertheless, assuming the Constant-Q model is valid over the whole frequency range, their results can still be related. Therefore the relationship between attenuation and composition is only indicative, and additional observations are needed to identify or distinguish regolith composition.

In general, low attenuation is associated with dry rocks, because saturation of rocks on Earth typically increases attenuation. Moreover, saturated rocks would also lower the propagation velocity substantially, below that observed in acquired RIMFAX data. As a consequence, this study is consistent with dry sedimentary rocks constituting the regolith of JWF.

Phyllosillicates have been identified at the JWF, both in orbital visible/near-infrared hyperspectral images (e.g., Horgan et al., 2020) and during surface operations by the Perseverance rover (Dehouck et al., 2023). Such minerals may contain bound water, and it has been hypothesized as a potential reason for high losses in orbital sounding elsewhere on Mars (Stillman & Grimm, 2011). But there is no indication of increased losses in the RIMFAX results from the Hawksbill Gap area, and therefore no indications of substantial amounts of bound water in phyllosilicates located in the upper 5–7 m of the regolith.

4. Conclusions

Attenuation in RIMFAX soundings from sols 439–538 and 698–709, acquired over the Jezero Western Fan Front (JWF Front), is estimated to $Q^* = 78.8 \pm 11.6$. That equals -2.1 ± 0.4 dB/m at the 675 MHz center frequency, for an average subsurface velocity of 0.113 m/ns. Results are a first look at the Hawksbill Gap area alone, and do not consider other parts investigated on JWF or nearby on the Crater Floor along the fan escarpment. Quantified attenuation estimates retrieved from the CFS method, are assessed and verified by comparing with the amplitude decay method. Results show that radar attenuation in the sedimentary deposits analyzed at JWF, is lower than over the magmatic lithologies investigated during sols 15–349 on the Crater Floor (where $Q^* = 70.4 \pm 7.7$ and $\alpha = -2.6 \pm 0.3$, with $v = 0.1$ m/ns). As a result, the maximum imaging depth increases by about 3 m at JWF.

Furthermore, the analysis does not indicate substantial amounts of brine or bound-water bearing minerals in the shallow subsurface, which would have increased attenuation and lowered the Q*-factor significantly.

Data Availability Statement

The data used in this work are available at the NASA PDS Geosciences Node (https://pds-geosciences.wustl.edu/missions/mars2020/rimfax.htm) (Hamran & Paige, 2021).

Acknowledgments
This work has received funding and support from the Research Council of Norway, Grant 309835 Centre for Space Sensors and Systems (CENSSS), through their SFI Centre for Research-based Innovation program.

References

Bogorodsky, V. V., Bentley, C. R., & Gudmandsen, P. (1985). *Radioglaciology* (Vol. 1). Springer Science & Business Media. https://doi.org/10.1007/978-94-009-5275-1

Bradford, J. H. (2007). Frequency-dependent attenuation analysis of ground-penetrating radar data. *Geophysics*, *72*(3), J7–J16. https://doi.org/10.1190/1.2710183

Campbell, B., Carter, L., Phillips, R., Plaut, J., Putzig, N., Safaeinili, A., et al. (2008). SHARAD radar sounding of the Vastitas Borealis Formation in Amazonis Planitia. *Journal of Geophysical Research: Planets*, *113*(E12). https://doi.org/10.1029/2008je003177

Casademont, T. M., Eide, S., Shoemaker, E. S., Liu, Y., Nunes, D. C., Russell, P., et al. (2023). RIMFAX ground penetrating radar reveals dielectric permittivity and rock density of shallow Martian subsurface. *Journal of Geophysical Research: Planets*, *128*(5), e2022JE007598. https://doi.org/10.1029/2022JE007598

Chen, R., Zhang, L., Xu, Y., Liu, R., Bugiolacchi, R., Zhang, X., et al. (2023). Martian soil as revealed by ground-penetrating radar at the Tianwen-1 landing site. *Geology*, *51*(3), 315–319. https://doi.org/10.1130/G50632.1

Dehouck, E., Forni, O., Quantin-Nataf, C., Beck, P., Mangold, N., Royer, C., & SuperCam Team. (2023). Overview of the Bedrock geochemistry and mineralogy observed by SuperCam during perseverance's delta front campaign. *54th lunar and planetary science conference*, *54*, 2862.

Ding, C., Xiao, Z., Su, Y., Zhao, J., & Cui, J. (2020). Compositional variations along the route of Chang'e-3 Yutu rover revealed by the lunar penetrating radar. *Progress in Earth and Planetary Science*, *7*(1), 1–11. https://doi.org/10.1186/s40645-020-00340-4

Eide, S., Casademont, T. M., Berger, T., Dypvik, H., Shoemaker, E. S., & Hamran, S.-E. (2022). Radar attenuation in the shallow Martian subsurface: RIMFAX time-frequency analysis and constant-Q characterization over Jezero Crater Floor. *Geophysical Research Letters*, *50*(7), e2022GL101429. https://doi.org/10.1029/2022GL101429

Eide, S., Hamran, S.-E., Dypvik, H., & Amundsen, H. E. (2021). Ground-penetrating radar modeling across the Jezero crater floor. *IEEE Journal of Selected Topics in Applied Earth Observations and Remote Sensing*, *14*, 2484–2493. https://doi.org/10.1109/JSTARS.2021.3055944

Farley, K. A., Stack, K. M., Shuster, D. L., Horgan, B. H. N., Hurowitz, J. A., Tarnas, J. D., et al. (2022). Aqueously altered igneous rocks sampled on the floor of Jezero crater, Mars. *Science*, *377*(6614), eabo2196. https://doi.org/10.1126/science.abo2196

Hamran, S.-E. (2010). Radar performance of ultra wideband waveforms. In G. Kouemou (Ed.), *Radar technology (Chap. 1)*. IntechOpen. https://doi.org/10.5772/7171

Hamran, S.-E., & Paige, D. A. (2021). Mars 2020 perseverance rover RIMFAX raw and calibrated data products [Dataset]. *NASA PDS Geosciences Node*. https://pds-geosciences.wustl.edu/missions/mars2020/rimfax.htm

Hamran, S.-E., Paige, D. A., Allwood, A., Amundsen, H. E. F., Berger, T., Brovoll, S., et al. (2022). Ground penetrating radar observations of subsurface structures in the floor of Jezero Crater, Mars. *Science Advances*, *8*(34), eabp8564. https://doi.org/10.1126/sciadv.abp8564

Hamran, S.-E., Paige, D. A., Amundsen, H. E., Berger, T., Brovoll, S., Carter, L., et al. (2020). Radar imager for Mars' subsurface experiment—Rimfax. *Space Science Reviews*, *216*(8), 1–39. https://doi.org/10.1007/s11214-020-00740-4

Harbi, H., & McMechan, G. A. (2012). Conductivity and scattering Q in GPR data: Example from the Ellenburger dolomite, central Texas. *Geophysics*, *77*(4), H63–H78. https://doi.org/10.1190/geo2011-0337.1

Horgan, B. H., Anderson, R. B., Dromart, G., Amador, E. S., & Rice, M. S. (2020). The mineral diversity of Jezero Crater: Evidence for possible lacustrine carbonates on Mars. *Icarus*, *339*, 113526. https://doi.org/10.1016/j.icarus.2019.113526

Irving, J. D., & Knight, R. J. (2003). Removal of wavelet dispersion from ground-penetrating radar data. *Geophysics*, *68*(3), 960–970. https://doi.org/10.1190/1.1581068

Lauro, S., Mattei, E., Cosciotti, B., Di Paolo, F., Arcone, S., Viccaro, M., & Pettinelli, E. (2017). Electromagnetic signal penetration in a planetary soil simulant: Estimated attenuation rates using GPR and TDR in volcanic deposits on Mount Etna. *Journal of Geophysical Research: Planets*, *122*(7), 1392–1404. https://doi.org/10.1002/2016je005192

Newman, P. (1973). Divergence effects in a layered earth. *Geophysics*, *38*(3), 481–488. https://doi.org/10.1190/1.1440353

Paige, D. A., Hamran, S.-E., Amundsen, H. E. F., Berger, T., Russell, P., Kakaria, R., et al. (2024). Ground penetrating radar observations of the contact between the western delta and the crater floor of Jezero Crater, Mars. *Science Advances*, *10*(4). https://doi.org/10.1126/sciadv.adi8339

Quan, Y., & Harris, J. M. (1997). Seismic attenuation tomography using the frequency shift method. *Geophysics*, *62*(3), 895–905. https://doi.org/10.1190/1.1444197

Richards, P. G., & Aki, K. (1980). *Quantitative seismology: Theory and methods* (Vol. 859). Freeman.

Stack, K. M., Ives, L. R. W., Gupta, S., Lamb, M. P., Tebolt, M., Caravaca, G., et al. (2024). Sedimentology and stratigraphy of the Shenandoah Formation, Western Fan, Jezero Crater, Mars. *Journal of Geophysical Research: Planets*, *129*(2), e2023JE008187. https://doi.org/10.1029/2023JE008187

Stack, K. M., Williams, N. R., Calef, F., Sun, V. Z., Williford, K. H., Farley, K. A., et al. (2020). Photogeologic map of the perseverance rover field site in Jezero Crater constructed by the Mars 2020 Science Team. *Space Science Reviews*, *216*(8), 1–47. https://doi.org/10.1007/s11214-020-00739-x

Stillman, D. E., & Grimm, R. E. (2011). Radar penetrates only the youngest geological units on Mars. *Journal of Geophysical Research*, *116*(E3), E03001. https://doi.org/10.1029/2010je003661

Tonn, R. (1991). The determination of the seismic quality factor Q from VSP data: A comparison of different computational methods. *Geophysical Prospecting*, *39*(1), 1–27. https://doi.org/10.1111/j.1365-2478.1991.tb00298.x

Turner, G., & Siggins, A. F. (1994). Constant Q attenuation of subsurface radar pulses. *Geophysics*, *59*(8), 1192–1200. https://doi.org/10.1190/1.1443677

Ulaby, F. T., & Long, D. G. (2014). *Microwave radar and radiometric remote sensing* (Vol. 4, p. 5). University of Michigan Press. https://doi.org/10.3998/0472119356